西安交通大学
XI'AN JIAOTONG UNIVERSITY

World Scientific
www.worldscientific.com

Optimization design of autofocusing metasurface for ultrasound wave application

Zhaoxi Li, Shenghui Yang, Mengqing Zhou, Chenxue Hou, Dongdong Chen,
Chunlong Fei[*], Di Li, Yi Quan and Yintang Yang

School of Microelectronics, Xidian University, Xi'an, Shaanxi 710071, P. R. China

*clfei@xidian.edu.cn

In this paper, two optimized autofocusing metasurfaces (AFMs) with different desired focal distances are designed by using particle swarm optimization (PSO) algorithm. Based on the finite element simulation software COMSOL Multiphysics, the performance of ultrasound transducer (UT) with AFM at different design parameters in Airy distributions (r_0, ω) and the bottom thickness (d) of AFM are simulated and analyzed. Based on the simulation data, the artificial neural network model is trained to describe the complex relationship between the design parameters of AFM and the performance parameters of UT. Then, the multiobjective optimization function for AFM is determined according to the desired performance parameters of UT, including focal position, lateral resolution, longitudinal resolution and absolute sound pressure. In order to obtain AFMs with the desired performance, PSO algorithm is adopted to optimize the design parameters of AFM according to the multiobjective optimization function, and two AFMs are optimized and fabricated. The experimental results well agree with the simulation and optimization results, and the optimized AFMs can achieve the desired performance. The fabricated AFM can be easily integrated with UT, which has great potential applications in wave field modulation underwater, acoustic tweezers, biomedical imaging, industrial nondestructive testing and neural regulation.

Keywords: Autofocusing; metasurface; ultrasound transducer; optimization.

1. Introduction

The manipulation of acoustic field plays an important part in many applications such as ultrasound imaging, nondestructive testing as well as cell and particle manipulation, and it can also be applied in wave focusing, which can improve the ability of biomedical imaging and realize the function of acoustic tweezers.[1–5] Phased array transducers, self-focusing mechanisms and acoustic lenses have been used to realize ultrasound focusing. Due to the nonlinear effects, the self-focusing mechanisms usually require large sound intensity.[6] Compared with phased array transducers, acoustic lens has the advantages of lower cost and higher efficiency.[7,8] Generally, focusing acoustic lenses include Fresnel lenses, curved solid lenses, acoustic liquid lenses, hologram, phononic crystal, acoustic metamaterials and metasurfaces.[9–19] Curved solid lenses are huge and hard to fabricate accurately. Acoustic metamaterials and metasurfaces have achieved unprecedented effective acoustic focusing by changing the thickness of the planar structures to adjust the phase delay in planar structures.[20–22] However, a large number of sub-wavelength units with complex microstructures are required to vary the phase from 0 to 2π to generate focused beams, which are hard to be fabricated, especially for biomedical ultrasound with typical wavelengths of millimeter order. Furthermore, traditional acoustic focusing lenses still stay in the low-frequency

acoustic wave manipulation with long focal length (FL) and difficult-to-achieve sharp beam autofocusing in both the lateral and axial directions under water. Efremidis and Christodoulides introduced a new class of optical waves which have enhanced autofocusing contrast and abruptness based on the Airy waves.[23] Chen *et al.* proposed an acoustic metasurface with good broadband acoustic focusing at 4 kHz based on the Airy source function.[24] Jiang *et al.* introduced a kind of ultrasound beam with sharp autofocusing properties based on the Airy functions at 500 kHz.[25] This structure has not only compact subsurface, but also sharp self-focusing. Although the Airy function is used to demonstrate the effective acoustic wave modulation for acoustic focusing, the relationship between the design parameters of acoustic metasurfaces and the performance of acoustic field based on Airy distributions is complex. Furthermore, traditional acoustic focusing analysis mainly studies plane waves of a single frequency, which requires a certain distance between the metasurfaces and the sound source. Therefore, the sound propagation loss and separation from the sound source limit its practical application. The optimization strategy of the design parameters of acoustic metasurfaces based on Airy distributions for ultrasonic focusing is rarely studied and reported.

Artificial intelligence (AI) has been widely used in many areas such as medicine, education, construction and finance

*Corresponding author.

to solve complicated modeling and optimization problems due to its high efficiency.[26,27] Artificial neural network (ANN) has been widely used in signal processing, data mining, pattern recognition, automatic control, prediction and many other fields due to its self-learning capacity, high efficiency and high robustness. In addition, as one of the intelligent optimization methods, particle swarm optimization (PSO) algorithm can efficiently obtain high-quality solution. PSO algorithm has been widely used in ANN training, function optimization, pattern classification and many other areas.[28] In addition, the optimization design of microdevices has been realized based on PSO algorithm.[29] Due to the advantages of AI methods in complex modeling and parameter optimization, they can be used to optimize the design parameters of acoustic metasurfaces for underwater wave focusing.

In this study, two acoustic autofocusing metasurfaces (AFMs) are designed based on Airy function at 1 MHz, and fabricated by 3D printing. The finite element simulation software COMSOL Multiphysics is used to simulate the performance of ultrasound transducers (UTs) with AFM at different design parameters, and then the simulation results are used to train the ANN model to accurately describe their relationship. PSO algorithm is used to optimize the design parameters of AFM according to the desired performance. All of the simulation, optimization and experimental results show a good focusing effect. The proposed AFM may have important applications in wave field modulation underwater, acoustic tweezers, biomedical imaging, industrial nondestructive testing and neural regulation.[30–32]

2. Experimental

2.1. Fabrication of the 3D printed AFM and ultrasonic transducers

The structures of the 3D printed AFMs with different design parameters are shown in Fig. 1. The AFM is made up of photosensitive resin and the 3D printing method of the AFM is
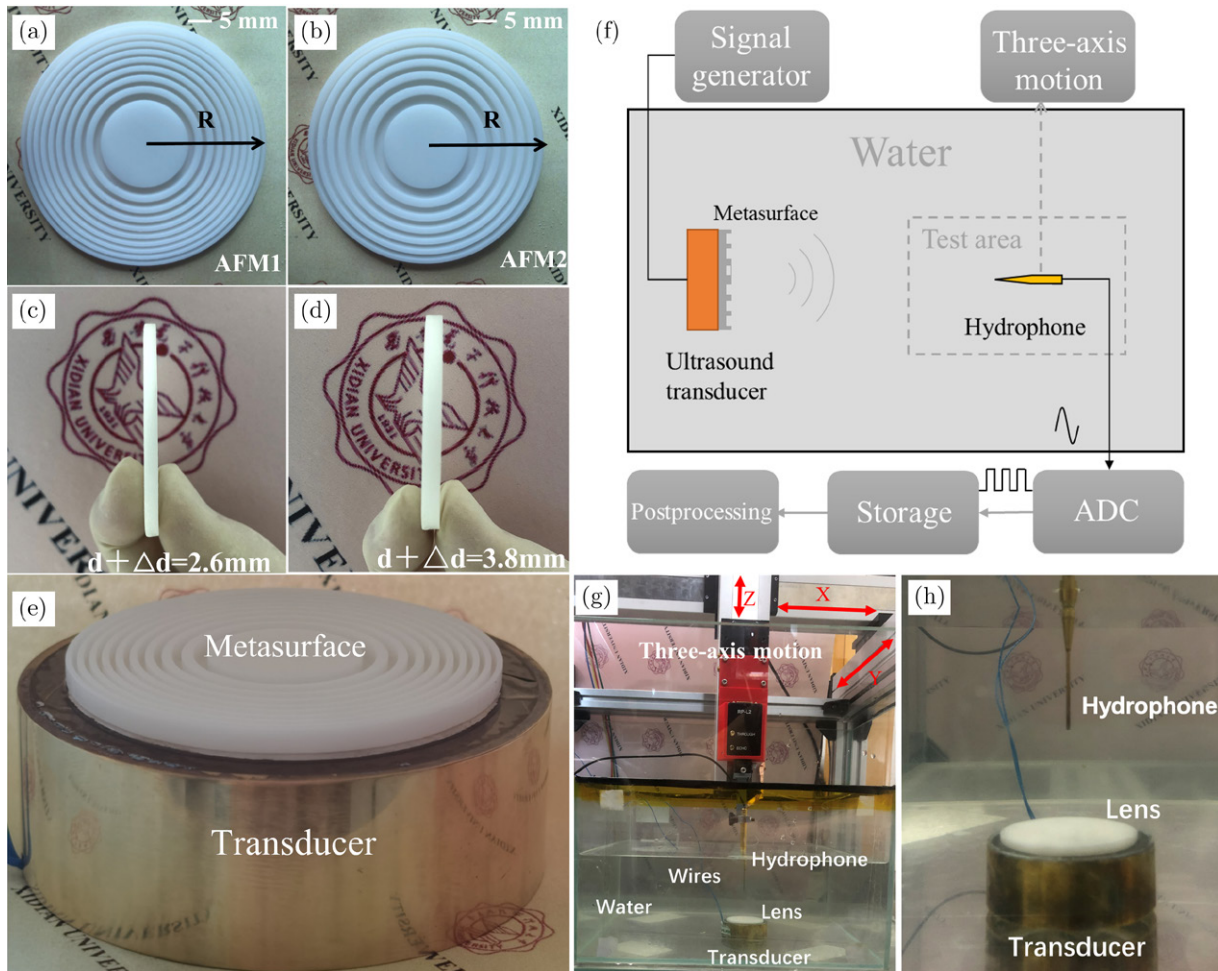

Fig. 1. The structures of the 3D printed AFMs (xy-plane): (a) AFM1 and (b) AFM2. The structures of the 3D printed AFMs (yz-plane): (c) AFM1 and (d) AFM2. The radii of the two fabricated AFMs are both 25 mm, the thicknesses of the 3D printed AFMs are 2.6 mm and 3.8 mm for AFM1 and AFM2, respectively. (e) The structure of the fabricated transducer. (f) The schematic diagram of hydrophone test pressure. (g) Side view of the experimental setup; and (h) zoomed-in side views of hydrophone, 3D printed metasurfaces and transducer.

high-precision projection micro-stereolithography (PμSL). The properties of the photosensitive resin are as follows: $\rho = 1300$ kg/m^3, velocity of the *P*-wave (c_p) = 2400 m/s and velocity of the *S*-wave (c_s) = 1000 m/s. Figure 1(e) shows the fabricated transducers made by a 2-mm-thick PZT-4 piezoelectric material with a diameter of 50 mm, and the working frequency of the transducer is 1 MHz. First, the piezoelectric material is sputtered with an Ag layer and connected to a copper wire. Second, the wired piezoelectric material is placed into a copper housing and fixed with potting epoxy. Then, the copper house is sputtered with another layer of Ag as the top electrode. Finally, the surface of transducer is coated with a layer of parylene for protection.

2.2. *Measurement of pressure fields*

Based on the optimized design parameters, as shown in Figs. 1(a)–1(d), the two AFMs are fabricated with photosensitive resin by a 3D printing technology. The experimental setup of the scanning system is given in Figs. 1(g) and 1(h) and the schematic diagram of the scanning system is shown in Fig. 1(f). The AFM is put on the surface of UT with a central frequency of 1 MHz, which was used to generate the incident sound waves along the lateral direction.

The pressure fields generated by the transducers were measured with a home-made scanning system based on LabVIEW. During the measurements, a sinusoidal pulse with 10 cycles at 1 MHz generated by an excitation generator (SMB100A, Rohde & Schwarz, Germany) and amplified by a 50-dB-power wideband amplifier (525LA, E&I, USA) was applied to the ultrasound transducer. Controlled by a stepping motor based on LabVIEW system, a hydrophone (NH1000, PA, UK) was used to measure the acoustic pressure field in a

50×30 mm^2 (*xz*-plane) rectangular area and a 50×50 mm^2 (*xy*-plane) rectangular area with an accuracy of 200 μm.

3. Results and Discussion

A sharp autofocusing ultrasound beam is given based on the circular Airy distribution of pressure on the initial plane $p(x,z = 0) = p_0(x)$, which is radially symmetric and described by Eq. (1),

$$p_0(x) = \mathrm{Ai}\left(\frac{r_0 - x}{\omega}\right)\exp\left(\alpha\,\frac{r_0 - x}{\omega}\right), \qquad (1)$$

where Ai($\cdot$) represents the Airy function, and r_0 is the initial radius of the primary ring. x is the radial distance, and ω is a scale factor with units of length. α ($\alpha = 0.05$ in this work) is an exponential decay factor to make sure that the wave transmits limited energy. The design parameters can affect the Airy function, and determine the shape of AFM, which finally determines the acoustic field.

Figure 2(a) shows the ultrasound focusing beam generated by the proposed AFM. Figure 2(b) shows the amplitude and phase profiles of the ideal pressure p_0 along the radial distance x based on the Airy distribution and Fig. 2(c) shows the phase and amplitude distributions based on the Airy distribution. In order to achieve a sharp focusing effect and simplify the manufacturing process, the Airy distributions with different parameters (r_0,ω) and the bottom thickness d of the AFM are optimized to form the phase distributions of 0 and $\mu\pi$ on the surface of the AFM. Here, a source plane of 2-bit Airy distribution is proposed, which inherits the phase distribution of p_0 but with unitary amplitude 1.

The distributions of phase (red) and amplitude (blue) as a function of x are given in Fig. 2(d). Figure 2(e) shows the
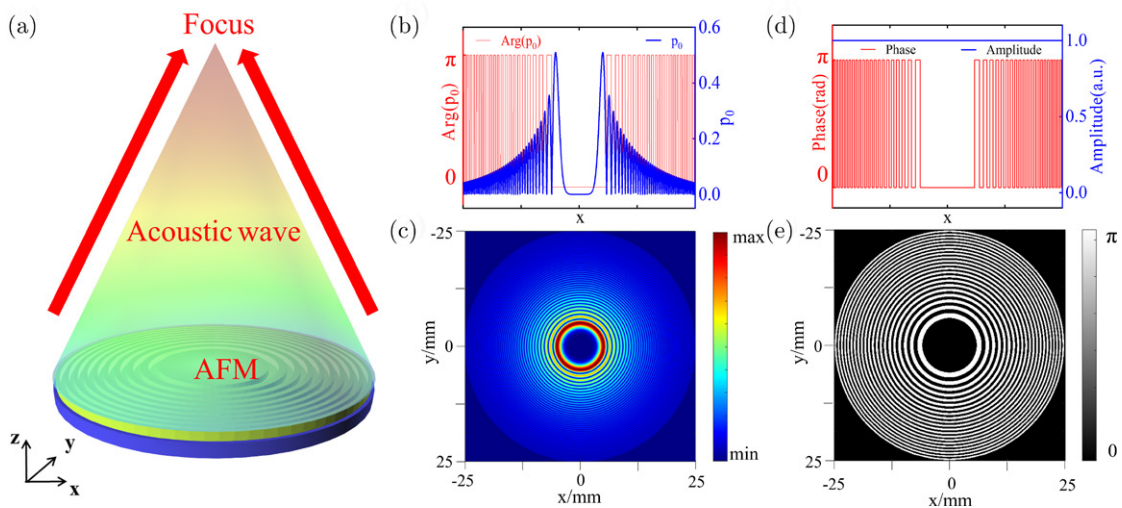

Fig. 2. (a) Ultrasound focusing beam generated by the proposed AFM. (b) The amplitude and phase profiles of the ideal pressure p_0 along the radial distance x based on the Airy distribution. (c) Designed phase and amplitude distributions based on the Airy distribution. (d) Designed phase and amplitude distributions along the radial distance x based on the 2-bit Airy distribution. (e) Designed phase distribution based on the 2-bit Airy distribution.

designed phase and amplitude distributions based on the 2-bit Airy distribution. Besides, experimental results demonstrate that the 2-bit Airy distribution with the phase-only modulation has nearly no influence on the sharp autofocusing properties. The transverse propagation of sound waves and the attenuation of acoustic waves in the thickness direction of AFM are not considered. The initial thickness of AFM is d_0. Removing material at the position (x,y) leads to a relative phase change, which can be described as shown in Eq. (2),

$$\Delta\phi(x, y) = (k_1 - k_2)\Delta d(x, y), \qquad (2)$$

where $d = d_0 - \Delta d(x,y)$ is the bottom thickness of AFM, and $\Delta d(x,y)$ is the thickness of the removed material at the coordinates (x,y) in the AFM. k_1 and k_2 are the wavenumbers in the AFM and its surrounding medium. In this work, the epoxy resin is chosen as the material of AFM, whose density is 1300 kg/m³, and its longitudinal wave velocity is 2400 m/s. The density of the surrounding medium (water) is 1000 kg/m³, and its longitudinal wave velocity is 1500 m/s. In order to form the phase distributions of 0 and π on the surface of AFM at 1 MHz, Δd is determined as 2 mm by Eq. (1). Figure 1(c)

is the picture of the 3D printed AFM, the finite element software COMSOL Multiphysics is used to simulate the focusing effect of the designed AFM. The axisymmetric model of the whole system is built in COMSOL Multiphysics, and the details are given in Fig. S1 in the Supplementary Material.

The performance of UT with AFM underwater is simulated by using COMSOL Multiphysics. UT is set as the sound source, and the AFM is placed on the surface of UT. The simulation results are given in Fig. S2 and Table S2 in the Supplementary Material. Obviously, the relationships between the design parameters (r_0,ω,d) and the performance parameters of UT are complicated. So, it is necessary to propose an effective way to determine the design parameters of AFM to achieve the designed focusing performance.

Figure 3(a) shows the 2D symmetric axial section of AFM, and ANN is used to describe the complicated relationship between the design and performance parameters of AFM due to its self-learning capacity, high robustness and high efficiency. The structure of ANN for r_0, ω and d is shown in Fig. 3(b). Figure 3(c) shows the simulated acoustic field distribution (xz-plane) of the AFM with UT. Figure 3(d)
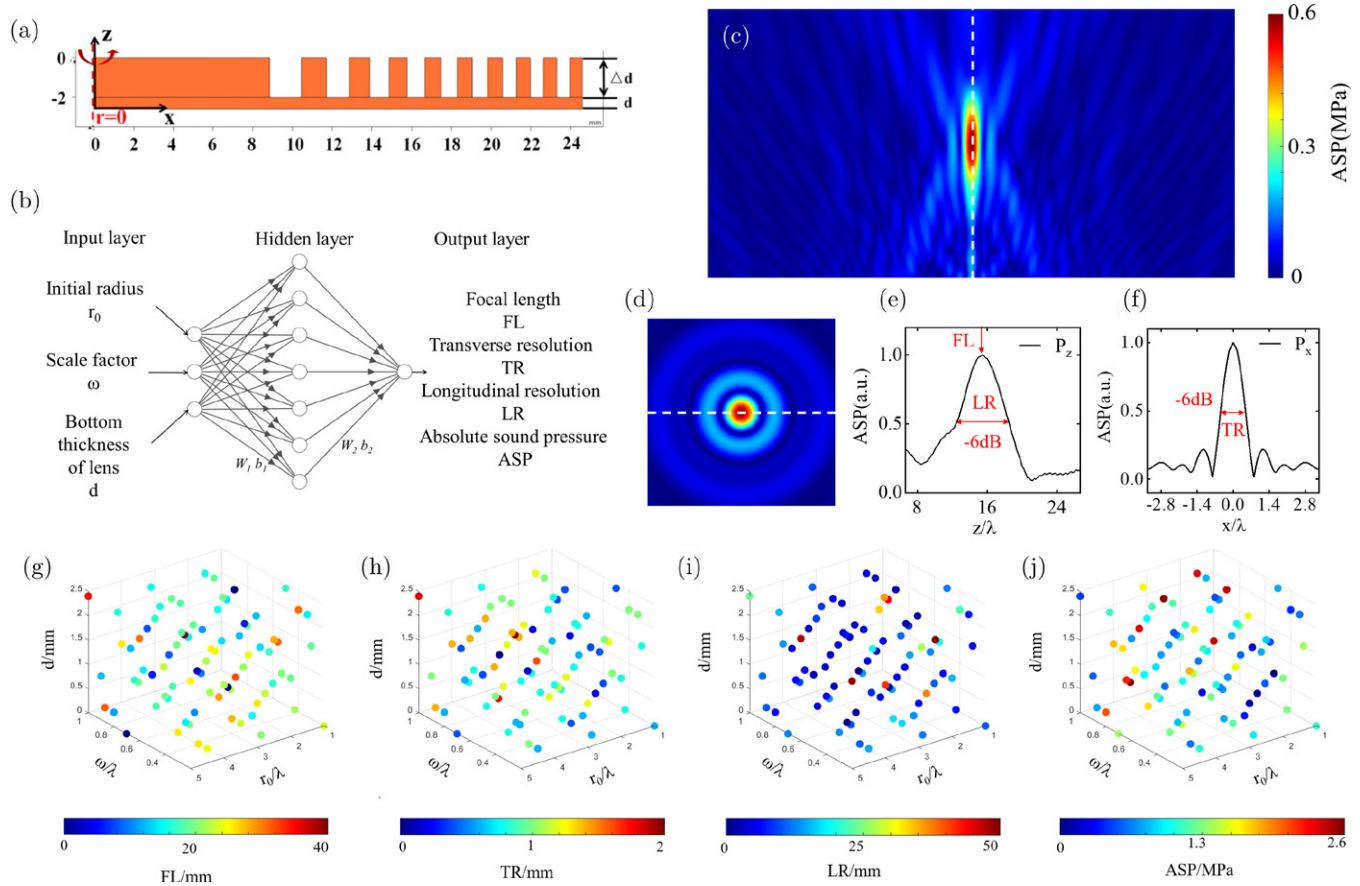

Fig. 3. (a) The 2D symmetric axial section of AFM. (b) Structure of ANN for AFM. (c), (d) The distributions of the simulated pressure amplitude of xz- and xy-planes. (e), (f) The normalized acoustic pressure distributions through the focal point along the longitudinal and lateral directions in panels (c) and (d) (white dotted lines), respectively. (g)–(j) The complex relationships between optimized design parameters and performance parameters.

shows the simulated sound field distribution near the focal point (*xy*-plane) of the AFM with UT. Figures 3(e) and 3(f) are the normalized acoustic pressure distributions through the focal point along the longitudinal and lateral directions in Figs. 3(c) and 3(d) (white dotted lines). Figures 3(g)–3(j) show the complex relationships between the optimized design and performance parameters. Obviously, it is necessary to propose an effective optimized method to describe the complex relationships between design parameters and performance parameters.

The equation for optimization design criterion of AFM can be described as follows:

$$J = \alpha J_{\mathrm{FL}} + \beta J_{\mathrm{TR}} + \gamma J_{\mathrm{LR}} + \delta J_{\mathrm{ASP}}, \quad (3)$$

where J_{FL}, J_{TR}, J_{LR} and J_{ASP} are the optimization criteria for FL, transverse resolution (TR), longitudinal resolution (LR) and absolute sound pressure (ASP), respectively. α, β, γ and δ are their weight coefficients.

In order to avoid the influence of performance parameters, the optimality criterion is normalized, and the normalized objective function is given as shown in Eq. (4),

$$J = \alpha\left(\frac{\mathrm{FL} - \mathrm{FL}_{\mathrm{des}}}{\mathrm{FL}_{\mathrm{max}} - \mathrm{FL}_{\mathrm{min}}}\right) + \beta\left(\frac{\mathrm{TR} - \mathrm{TR}_{\mathrm{des}}}{\mathrm{TR}_{\mathrm{max}} - \mathrm{TR}_{\mathrm{min}}}\right)$$
$$+ \gamma\left(\frac{\mathrm{LR} - \mathrm{LR}_{des}}{\mathrm{LR}_{\mathrm{max}} - \mathrm{LR}_{\mathrm{min}}}\right) + \delta\left(\frac{\mathrm{ASP} - \mathrm{ASP}_{des}}{\mathrm{ASP}_{\mathrm{max}} - \mathrm{ASP}_{\mathrm{min}}}\right), \quad (4)$$

where $\mathrm{FL}_{\mathrm{max}}$, $\mathrm{FL}_{\mathrm{min}}$, $\mathrm{TR}_{\mathrm{max}}$, $\mathrm{TR}_{\mathrm{min}}$, $\mathrm{LR}_{\mathrm{max}}$ and $\mathrm{LR}_{\mathrm{min}}$ are the maximum and minimum values of FL, TR and LR, respectively.

The parameters of the optimization design method for AFM with different performance targets are shown in Table 1. In order to make the optimization results of the four parameters of FL, TR, LR and ASP approach the initial target values, here we choose all the weight coefficients as 0.25 to reduce each parameter with a larger difference. For AFM1, the desired FL, TR, LR and ASP are 30 mm, 1.5 mm, 8 mm and 2 MPa, respectively. For AFM2, the desired FL, TR, LR and ASP are 25 mm, 1.4 mm, 10 mm and 2.5 MPa, respectively. The maximum generations and population size of PSO algorithm are 50 and 20 to ensure the accuracy of the optimized results. In order to reduce the influence of random errors of PSO algorithm, the proposed method has been independently run 30 times. Table S3 in Supplementary Material shows the optimized design parameters of AFM1 and the corresponding performance parameters. The optimized design parameters are shown in Figs. S2(a)–S2(c) in Supplementary Material. The optimized r_0, ω and d of AFM1 are 4.5λ, 0.6λ and 0.6 mm, respectively, where $\lambda = 1.5$ mm (frequency: 1 MHz). Figures S3(a)–S3(d) in Supplementary Material show the performance parameters of UT with AFM1 under the optimized design parameters. The optimized TR, LR, FL and pressure amplitude ASP of 30 runs are similar, which implies that the developed method is effective and stable. The obtained TR,

Table 1. Parameters of the optimization design method.

Case		AFM1	AFM2
Parameters of optimality criteria	Desired focal length (mm)	30	25
	Desired transverse resolution (mm)	1.5	1.4
	Desired longitudinal resolution (mm)	8	10
	Desired absolute sound pressure (MPa)	0.02	0.025
	Weight coefficients	$\alpha = 0.25$, $\beta = 0.25$, $\gamma = 0.25$, $\delta = 0.25$	
Parameters of PSO-LDIW algorithm	Constant parameters	$c_1 = 2$, $c_2 = 2$	
	Range of inertia weight	Weight $\in [0.4, 0.9]$	
	Maximum generation	MaxG = 50	
	Population size	$N = 20$	
	Range of particle position	$r_0 \in [1,5]$, $\omega \in [0.2,1]$, $d \in [0,2.4]\,\lambda$	
	Range of particle velocity	$v_{r0} \in [-1, 1]\,\lambda$, $v_\omega \in [-0.1, 0.1]\,\lambda$, $v_d \in [-1, 1]\,\lambda$	

LR, FL and ASP for AFM1 are about 1.499 mm, 8.203 mm, 30 mm and 1.99 MPa, respectively, which keeps good consistency with the designed performance.

Table S4 in Supplementary Material shows the optimized design parameters of AFM2 and the corresponding performance parameters. The optimized design parameters are shown in Figs. S4(a)–S4(c) in Supplementary Material. The optimized r_0, ω and d of AFM2 are 4λ, 0.8λ and 1.8 mm, respectively, where $\lambda = 1.5$ mm (frequency: 1 MHz). Figures S5(a)–S5(d) in Supplementary Material show the performance parameters of UT with AFM2 under the optimized design parameters. Also, the optimized TR, LR, FL and ASP of 30 runs are similar, which are about 1.399 mm, 10.239 mm, 25.051 mm and 2.49 MPa, respectively, and the obtained performance well agrees with the designed performance. Obviously, the whole optimization results are relatively stable, and the errors of few points are caused by the random disturbance during the optimization process, which indicates that the optimized results are reliable and reasonable.

The ANNs for r_0, ω and d are trained based on the simulation results, as shown in Table 2. The prediction performance results and the simulation results show good consistency. The proposed ANNs can precisely describe the complex relationships between design parameters and the performance of AFM.

The simulated underwater field distributions of UT in the plane $y = 0$ with AFM1 are shown in Fig. 4(a). Figures 4(b) and 4(c) are the experimental field cross-section distributions (10 mm × 10 mm) in Fig. 4(a) (red dotted lines) and the experimental transversal field magnitude distributions
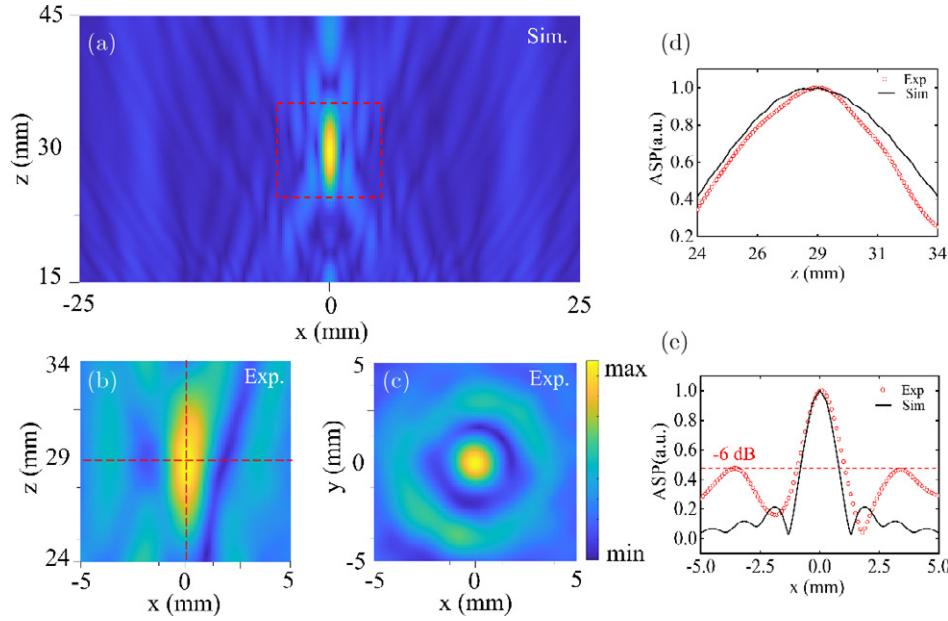
Fig. 4. (Color online) (a) The simulated underwater field distributions of UT in the plane $y = 0$ with AFM1. (b) The experimental field cross-section distributions in panel (a) (red dotted lines). (c) The experimental transversal field magnitude distributions (*xy*-plane) of UT with AFM1 at the focal point. (d), (e) The normalized acoustic pressure distributions through the focal point along the longitudinal and lateral directions in panel (b) (red dotted lines).
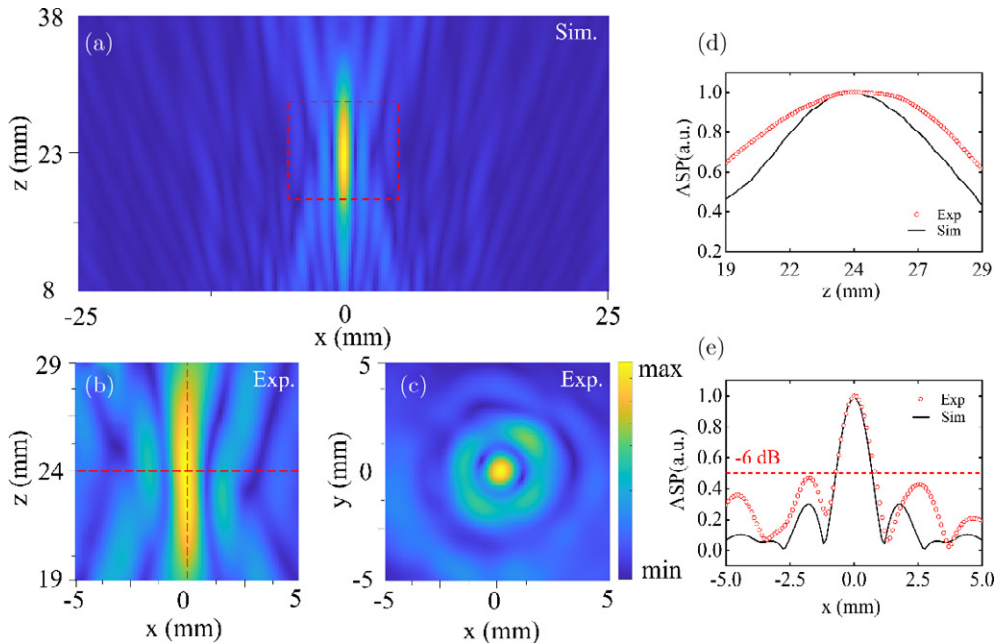

Fig. 5. (Color online) (a) The simulated underwater field distributions of UT in the plane $y = 0$ with AFM2. (b) The experimental field cross-section distributions in panel (a) (red dotted lines). (c) The experimental transversal field magnitude distributions (xy-plane) of UT with AFM2 at the focal point. (d), (e) The normalized acoustic pressure distributions through the focal point along the longitudinal and lateral directions in panel (b) (red dotted lines).

(10 mm × 10 mm; *xy*-plane) of UT with AFM1 at the focal point. Figures 4(d) and 4(e) are the normalized acoustic pressure distributions through the focal point along the longitudinal and lateral directions in Fig. 4(b) (red dotted lines).

The simulated and experimental underwater field distributions of UT with AFM2 are shown in Fig. 5. The simulation and experimental results of lateral resolution TR (−6 dB), vertical resolution LR (−6 dB), focal point FL and pressure

Table 2. Optimization, simulation and experimental results of UTs with AFMs.

AFM1	TR (mm)	LR (mm)	FL (mm)	ASP (MPa)
Optimization	1.499	8.203	30	1.99
Simulation	1.5	8.76	30	1.985
Experimental	1.9	7.78	28.546	1.947

AFM2	TR (mm)	LR (mm)	FL (mm)	ASP (MPa)
Optimization	1.399	10.239	25.051	2.49
Simulation	1.4	9.12	23.24	2.55
Experimental	1.5	13.56	24.676	2.80

amplitude of optimization are given in Table 2. The experimental results of AFM well agree with the optimization and simulation results. The existence of shear waves, printing error and the attenuation of sound waves in the thickness direction of AFM may account for little difference in the performance between experimental and simulation results. AFM1 shows longer focal length and higher vertical resolution but lower acoustic pressure at the focal point than AFM2. Therefore, the ultrasonic transducer with AFM1 is suitable for neuromodulation and acoustic tweezer applications. On the other hand, AFM2 achieves high ultrasound energy and long focal depth, which may improve the ultrasound imaging or nondestructive testing.

4. Conclusion

In this work, an efficient optimization strategy is developed to design the AFM based on Airy distributions for UT, based on ANN and PSO algorithm. According to the designed targets, two AFMs are designed and fabricated by 3D printing. The FL, TR, LR and ASP of UT with AFM1 are 28.546 mm, 1.9 mm, 7.78 mm and 1.947 MPa, and those of AFM2 are 24.676 mm, 1.5 mm, 13.56 mm and 2.8 MPa, demonstrating that sharp focusing effects underwater can be achieved by using the designed AFMs. In addition, the optimization, simulation and experimental results have good consistency, which validates the effectiveness of the developed optimization strategy. Therefore, the AFMs with desired performance can be designed by the developed method, and have important applications in wave field modulation underwater, acoustic tweezers, biomedical imaging, industrial nondestructive testing and neural regulation.

References

[1] K. Shung, High frequency ultrasonic imaging, *J. Med. Ultrasound* **17**, 25 (2009).

[2] Q. Zhou, K. Lam, H. Zheng, W. Qiu and K. Shung, Piezoelectric single crystal ultrasonic transducers for biomedical applications, *Prog. Mater. Sci.* **66**, 87 (2014).

[3] L. Le Jeune, S. Robert, E. Lopez Villaverde and C. Prada, Plane wave imaging for ultrasonic non-destructive testing: Generalization to multimodal imaging, *Ultrasonics* **64**, 128 (2016).

[4] M. Baudoin, J. Thomas, R. Sahely, J. Gerbedoen, Z. Gong, A. Sivery, O. Matar, N. Smagin, P. Favreau and A. Vlandas, Spatially selective manipulation of cells with single-beam acoustical tweezers, *Nat. Commun.* **11**, 4244 (2020).

[5] L. Jiang, H. Chen, Y. Zeng, Z. Tan, J. Wu, J. Xing and J. Zhu, Potassium sodium niobate-based lead-free high-frequency ultrasonic transducers for multifunctional acoustic tweezers, *ACS Appl. Mater. Interfaces* **14**, 30979 (2022).

[6] C. Klingshirn, J. Fallert, H. Zhou and H. Kalt, Comment on "Excitonic ultraviolett lasing in ZnO-based light emitting devices", *Appl. Phys. Lett.* **91**, 126101 (2007).

[7] Y. Yang, T. Ma, S. Li, Q. Zhang, J. Huang, Y. Liu, J. Zhuang, Y. Li, X. Du, L. Niu, Y. Xiao, C. Wang, F. Cai and H. Zheng, Self-navigated 3D acoustic tweezers in complex media based on time reversal, *Research* **2021**, 9781394 (2021).

[8] A. Marzo and B. W. Drinkater, Holographic acoustic tweezers, *Proc. Natl. Acad. Sci. USA* **116**, 84 (2019).

[9] M. Molerón, M. Serra-Garcia and C. Daraio, Acoustic Fresnel lenses with extraordinary transmission, *Appl. Phys. Lett.* **105**, 114109 (2014).

[10] P. Peng, B. Xiao and Y. Wu, Flat acoustic lens by acoustic grating with curled slits, *Phys. Lett. A* **378**, 3389 (2014).

[11] Z. Li, R. Guo, C. Fei, D. Li, D. Chen, C. Zheng, R. Wu, W. Feng and Y. Yang, Liquid lens with adjustable focus for ultrasonic imaging, *Appl. Acoust.* **175**, 107787 (2021).

[12] K. Melde, A. Mark, T. Qiu and P. Fischer, Holograms for acoustics, *Nature* **537**, 518 (2016).

[13] S. Jiménez-Gambín, N. Jiménez, J. Benlloch and F. Camarena, Holograms to focus arbitrary ultrasonic fields through the skull, *Phys. Rev. Appl.* **12**, 014016 (2019).

[14] Z. Li, S. Yang, D. Wang, H. Shan, D. Chen, C. Fei, M. Xiao and Y. Yang, Focus of ultrasonic underwater sound with 3D printed phononic crystal, *Appl. Phys. Lett.* **119**, 073501 (2021).

[15] A. Allam, K. Sabra and A. Erturk, 3D-printed gradient-index phononic crystal lens for underwater acoustic wave focusing, *Phys. Rev. Appl.* **13**, 064064 (2020).

[16] J. Liu, Z. Li, Y. Ding, A. Chen, B. Liang, J. Yang, J. Cheng and J. Christensen, Twisting linear to orbital angular momentum in an ultrasonic motor, *Adv. Mater.* **34**, 2201575 (2022).

[17] G. Liao, C. Luan, Z. Wang, J. Liu, X. Yao and J. Fu, Acoustic metamaterials: A review of theories, structures, fabrication approaches, and applications, *Adv. Mater. Technol.* **6**, 2000787 (2021).

[18] S. A. Cummer, J. Christensen and A. Alù, Controlling sound with acoustic metamaterials, *Nat. Rev. Mater.* **1**, 16001 (2016).

[19] B. Xie, K. Tang, H. Cheng, Z. Liu, S. Chen and J. Tian, Metasurfaces: Coding acoustic metasurfaces, *Adv. Mater.* **29**, 1603507 (2017).

[20] Y. Li, G. Yu, B. Liang, X. Zou, G. Li, S. Cheng and J. Cheng, Three-dimensional ultrathin planar lenses by acoustic metamaterials, *Sci. Rep.* **4**, 6830 (2014).

[21]Y. Ding, E. Statharas, K. Yao and M. Hong, A broadband acoustic metamaterial with impedance matching layer of gradient index, *Appl. Phys. Lett.* **110**, 241903 (2017).

[22]X. Jiang, B. Liang, R. Li, X. Zou, L. Yin and J. Cheng, Ultra-broadband absorption by acoustic metamaterials, *Appl. Phys. Lett.* **105**, 243505 (2014).

[23]N. Efremidis and D. Christodoulides, Abruptly autofocusing waves, *Opt. Lett.* **35**, 4045 (2010).

[24]D. Chen, X. Zhu, Q. Wei, D. Wu and X. Liu, Broadband acoustic focusing by Airy-like beams based on acoustic metasurfaces, *J. Appl. Phys.* **123**, 044503 (2018).

[25]X. Jiang, Y. Li, D. Ta and W. Wang, Ultrasonic sharp autofocusing with acoustic metasurface, *Phys. Rev. B* **102**, 064308 (2020).

[26]W. Zhang, Z. Zhang, S. Zeadally, H.-C. Chao and V. C. M. Leung, MASM: A multiple-algorithm service model for energy-delay optimization in edge artificial intelligence, *IEEE Trans. Ind. Inform.* **15**, 4216 (2019).

[27]P. Mach and Z. Becvar, Mobile edge computing: A survey on architecture and computation offloading, *IEEE Commun. Surv. Tutor.* **19**, 1628 (2017).

[28]D. Chen and Y. Lin, A particle swarm optimization-based multi-level processing parameters optimization method for controlling microstructures of an aged superalloy during isothermal forging, *Met. Mater. Int.* **25**, 1246 (2019).

[29]D. Chen, C. Hou, C. Fei, D. Li, P. Lin, J. Chen and Y. Yang, An optimization design strategy of 1–3 piezocomposite ultrasonic transducer for imaging applications, *Mater. Today Commun.* **24**, 100991 (2020).

[30]T. Zhang, H. Liang, Z. Wang, C. Qiu, Y. Peng, X. Zhu, J. Li, X. Ge, J. Xu, X. Huang, J. Tong, J. Ou-Yang, X. Yang, F. Li and B. Zhu, Piezoelectric ultrasound energy-harvesting device for deep brain stimulation and analgesia applications, *Sci. Adv.* **8**, eabk0159 (2022).

[31]Z. Li, D. Wang, C. Fei, Z. Qiu, C. Hou, R. Wu and Y. Yang, The forbidden band and size selectivity of acoustic radiation force trapping, *iScience* **24**, 101988 (2021).

[32]H. Salahshoor, M. Shapiro and M. Ortiz, Transcranial focused ultrasound generates skull-conducted shear waves: Computational model and implications for neuromodulation, *Appl. Phys. Lett.* **117**, 033702 (2020).